Quan Yuan, B. G. Thomas, and S. P. Vanka, ISSTech 2003 (Conf. Proc.), Indianapolis, IN, USA, Apr. 27-30, 2003, ISS-AIME, Warrendale, PA, 2003, pp. 913-927.

Turbulent Flow and Particle Motion in Continuous Slab-Casting Molds

Quan Yuan, Brian G. Thomas and S. P. Vanka

Mechanical and Industrial Engineering Department
University of Illinois at Urbana-Champaign
1206 W. Green St., Urbana, IL 61801, USA
Tel.: (217) 244-2859, (217) 333-6919
E-mail: quanyuan@uiuc.edu, bgthomas@uiuc.edu, s-vanka@uiuc.edu

Key Words: Fluid flow, turbulence, large eddy simulation (LES), particle, continuous casting molds, steel

INTRODUCTION

Turbulent flow in the continuous casting process involves transient phenomena and the transport of inclusion particles and plays an important role in the quality of the steel. As shown in Fig. 1, the molten steel jet entering the mold may carry inclusion particles (e.g. alumina) and argon bubbles. Liquid flux can also be entrained from the shear of the liquid flow across the top surface and form harmful inclusions. These inclusions and bubbles will either be safely transported to the top surface and removed by the slag layer, or become entrapped in the final product to form costly defects (e.g. internal porosity, blisters, slivers etc.). The flow in the mold region is highly turbulent with Reynolds numbers exceeding 100,000. The chaotic structures of this transient flow greatly influence the unsteady transport of the inclusions and bubbles, which has been evidenced by intermittent defects in plant observation [1]. This transient flow itself is also of great interest for being associated with other defects. The time-varying top surface level, for instance, changes the thickness of the liquid flux layer covering the molten steel, and further affects the steady supply of liquid flux into the interfacial gap between the shell and mold. Sudden level fluctuations are associated with surface cracks and other defects in plant studies. The present study is part of a larger ongoing research project to investigate the transient structures of this mold flow and inclusion particle behavior with the objective of understanding and minimizing these defects.

Extensive studies have used Reynolds averaged turbulence models (mainly k-ε model) to understand this flow [2-7]. Models accounting for turbulence effects on particle motion (e.g. random-walk model) have been employed to study particle behavior [7]. The computational cost of these models is feasible for engineering applications, but their accuracy has not been benchmarked for this complex multiphase flow. This project aims at understanding the physics of this chaotic flow and particle behavior, and based on this to develop more accurate and efficient mathematical models for this multiphase flow. Large Eddy Simulation (LES), which is more accurate than the k-ε model for resolving the evolution and dynamics of the large-scale turbulence structures, has been recently employed to study turbulent flow during continuous casting [8-10]. Though accurate and capable of generating powerful insights into transient flow phenomena, when it is applied to this complex flow problem, many challenges arise, including the prescription of transient inlet conditions, resolution of the velocity and thermal boundary layers, the moving solidifying front and the long-term transients. Thus the LES simulations are complicated and require large computer memory and CPU time. LES is thus best suitable as a tool for benchmarking other engineering models.

Measurements in steel casting machines are difficult and expensive, due to the high operating temperature. Because of nearly equal kinematic viscosities of the molten steel and water, flow in steel casters has been studied using scaled water models [11-13], which are easier to operate and allow flow visualization. Recently, we applied Particle Image Velocimetry (PIV), probably the most accurate 2D flow velocity measurement technique, to study the flow in a 0.4-scaled water model [8]. The prediction of our LES code has been compared with the measured data to have a favorably good agreement [8].

Although very valuable, the water model differs from the real casting machine in several aspects important to fluid flow. First, the sidewalls, which represent the moving solidifying shell, are non-porous and stationary. Further, the water model has a flat bottom with outlet ports instead of the tapering molten steel pool. These two major differences lead to different flow phenomena, which are investigated here.

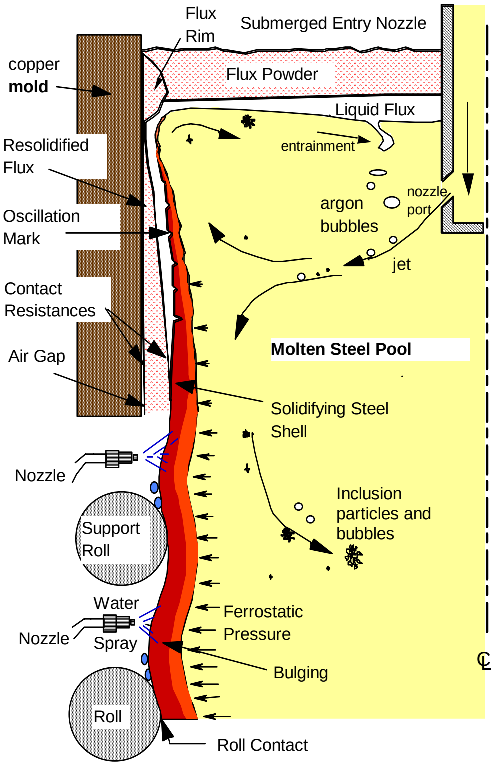

Fig. 1: Schematic of flow phenomena in mold region of continuous casting process.

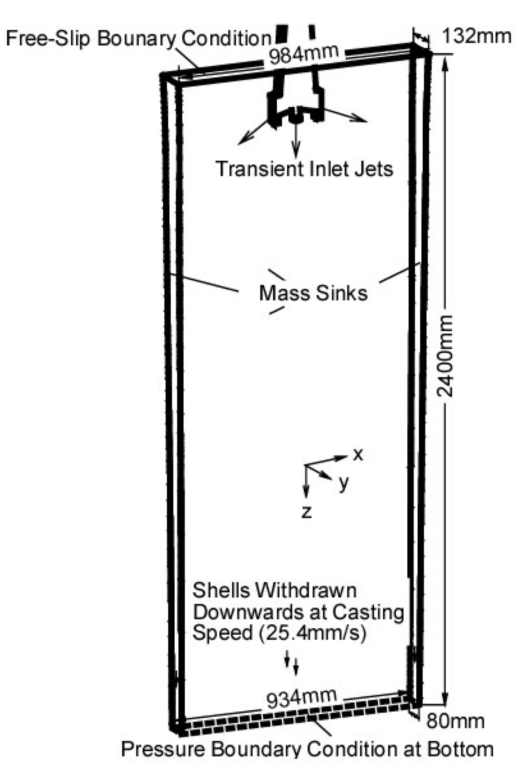

Fig. 2: Schematic of the computational domain of the steel caster.

This paper presents results from two mold flow simulations, including inclusion particle transport and entrapment computations. Our previous work [6] found that accurately prescribing the time-varying velocities exiting the nozzle ports, which are the inlet conditions for the mold simulations, is important to accurately computing the flow in the mold. Therefore before the mold simulations, the flow in a corresponding nozzle (see Fig. 2), which is in use during plant operations, was computed using CART3D (in-house LES code, with 6.3×10^5 computational cells). The velocities at the nozzle ports were stored every 0.025s for 9.45s (10-day computation on PentiumIV 1.7GHz CPU) to serve as the transient inlet velocities of the mold simulations by recycling periodically. Detailed information of this nozzle geometry and the simulation can be found elsewhere [14]. CART3D is then employed to simulate the flow in a full-scale water model and a corresponding steel casting machine which has been measured carefully in previous work [14-16]. The effects of solidification and downward withdrawal of the shell are mathematically modeled in the steel caster simulation. Accompanying the fluid flow simulation, the transport of four groups of different property alumina particles (e.g. representing different liquid steel content fraction) is simultaneously computed in the steel caster using "one-way coupling" (particles are transported by fluid flow but the fluid flow is not affected by the particles).

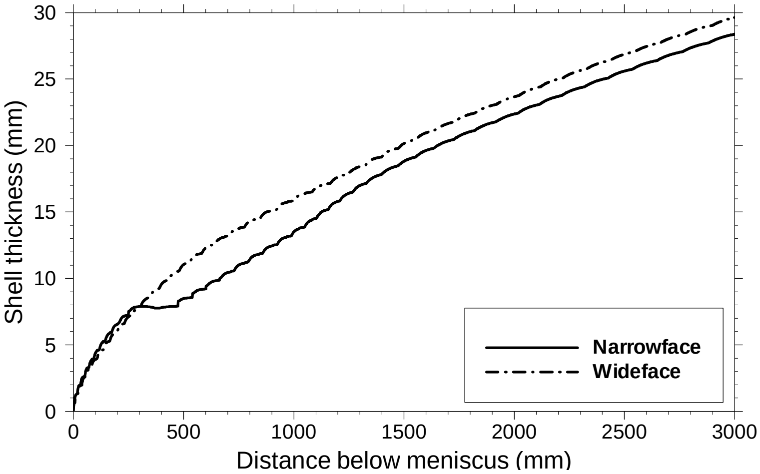

Fig. 3: Predicted shell thickness.

Figure 2 shows the computational domain of the steel casting machine. The curved shape of the side boundaries represents the solidifying shell front at the liquidus temperature. The shell thickness shown in Fig. 3 was calculated by Y. Meng using an in-house code CON1D [17] developed at the Metal Processing Lab of University of Illinois at Urbana-Champaign. Note that CON1D includes the effect of jet impingement, which shows shell growth on the narrow faces. Source terms for the mass and momentum across the boundary were implemented into CART3D at the shell boundaries to represent the effect of solidification and downward withdrawal of the shell. The computational domain of the water model is slightly different in that its sidewalls are vertically straight and stationary. Its height is half that of the domain for the steel caster simulation. The geometry of the water model and steel caster molds and computational domains are shown in Table I, together with the casting conditions and material properties.

Table I. Properties and conditions of LES simulations.

Parameter/Property	Water Model	Steel Caster
Mold Width (mm)	984	984
Mold Thickness (mm)	132	132
Water Model Length (mm)	2600	-
Mold Length (mm)	-	1200
Domain Width (mm)	984	984 (top) 934.04 (domain bottom)
Domain Thickness (mm)	132	132 (top) 79.48 (domain bottom)
Domain Length (mm)	1200	2400
Nozzle Port Height × Thickness (mm × mm)	75 × 32 (inner bore)	75 × 32 (inner bore)
Bottom nozzle Port Diameter (mm)	32	32
SEN Submergence Depth (mm)	127	127
Casting Speed (mm/s)	25.4	25.4
Dynamic Viscosity of Liquid Steel (m^2/s)	1.0×10^{-6}	7.98×10^{-7}

The simulations are first compared with measurements and favorable agreement is seen. Results of this study show transient flow asymmetry in both the top surface (top surface velocity and surface level) and lower roll zone (downward velocity). This consequently causes the asymmetry of the particle transport and entrapment. Two-side interaction of the caster is found to cause of the flow asymmetry. Flow in the steel caster is found to likely have more evenly distributed downward velocities than the water model. This work also shows that the top surface level can be reasonably approximated using the computed top surface pressure distribution. Particle transport features, trajectories and entrapment locations are finally investigated.

FLUID FLOW RESULTS

Comparison of LES and Measurements

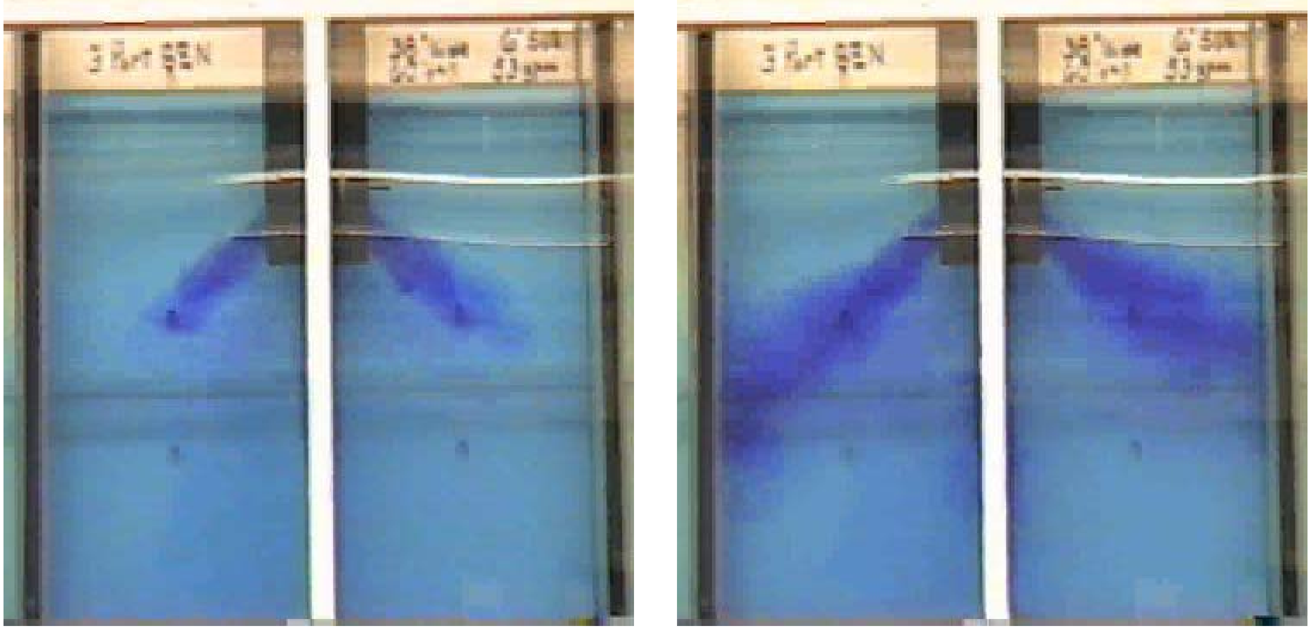

(a) 0.5 seconds (b) 1.2 seconds

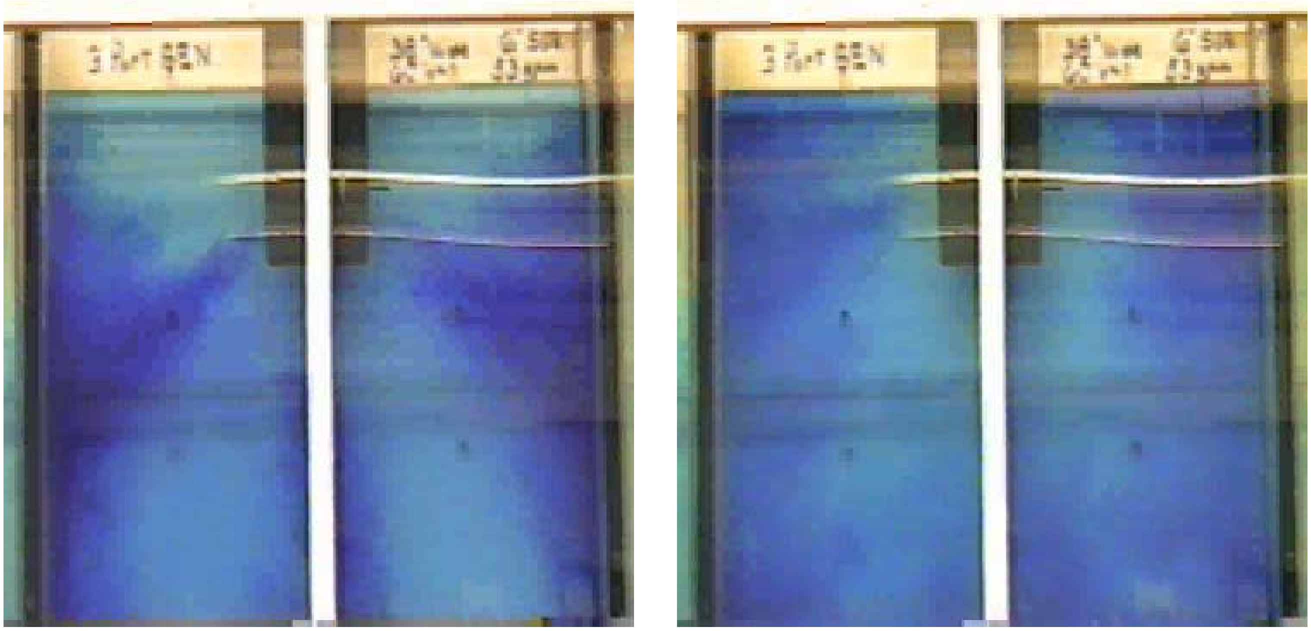

(c) 2.8 seconds (d) 5.1 seconds

Fig. 4: Dye injection showing the flow in the water model mold region at four instants.

Figure 4 presents snap shots of the dye injection experiment on the full-scale water model at four instants, showing the evolution of the transient flow in the mold region. Figure 4(a) is 0.5 seconds after the dye exits the nozzle ports, showing instantaneous jet angles of ~42^o (left) and ~35^o (right). The dye flows along the jet and hits the narrow face 0.7 seconds later as shown in Fig. 4(b). The dye then splits into two parts with the flow to move into the lower and upper roll zones, as can be seen in plots (c) and (d). The shape of the jets, the lower and upper rolls can be reconstructed from the sequence of the four plots. The vortex shedding asymmetries of the center jet can also be observed, although they are obscured somewhat by part of the external frame of the water model.

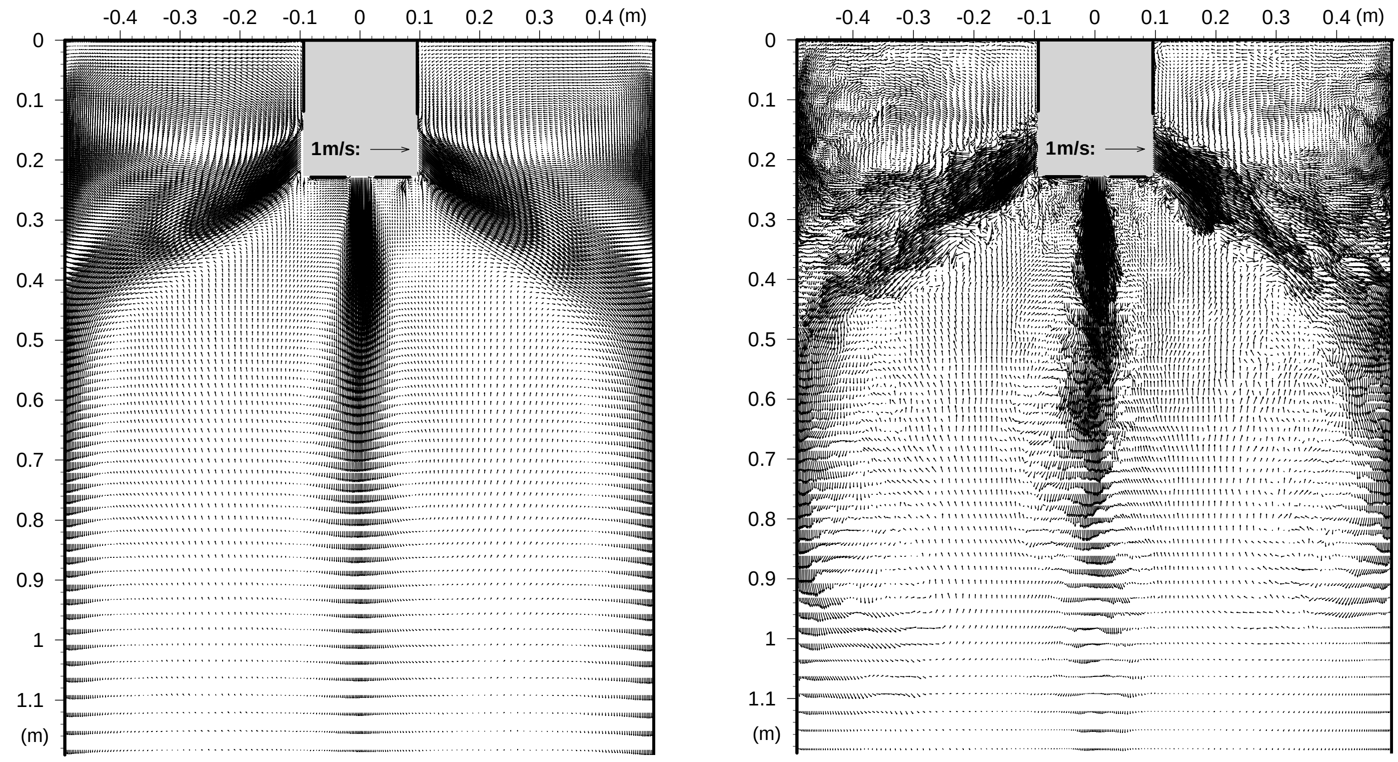

(a) (b)

Fig. 5: LES predicted (a) time-averaged and (b) typical instantaneous velocity vectors at the center plane of the full-scale water model.

The computed velocity field of this water model is shown in Fig. 5, and can be compared with the dye injection measurements. The two figures present the time-averaged and typical instantaneous velocity vector plots at the center plane between widefaces respectively. In both plots, the classical double roll flow pattern can be seen. The shape of the jets, the upper and lower rolls agrees with the dye-injection. Opposed to the smooth time-averaged velocity vectors, the instantaneous velocity vector plot shows chaotic local turbulent structures, which evolve with time as seen by checking instantaneous sequences. The vortex shedding of the center jet observed in the dye injection can also be seen in the calculated instantaneous plots. The time-averaged and instantaneous velocity fields of the steel caster, obtained from LES, are shown in Fig. 6 to be qualitatively similar as the water model. It should be noted that for both the water model and steel caster, a slight asymmetry exists in the time-averaged central jet, which are averaged over 48.5 and 51 seconds respectively. This asymmetry indicates a low frequency oscillation between two sides exists in the central jet, which might lead to transient asymmetry defects observed in the plant. The flow asymmetry and its consequent effect will be discussed in more detail later.

Figure 7 compares LES with the dye injection measurements in the water model. The solid line shows the flow speed $(v_x^2 + v_y^2)^{1/2}$ along the jet centerline obtained from the LES average data (over 48.5 and 51 seconds for the water model and steel caster respectively). The error bars are the predicted highest and lowest transient speeds during the 48.5 and 51 seconds simulations respectively, showing a wide range fluctuation of the jet speed. The dark dots present the approximated flow speed obtained by measuring the dye front motion speed on the video. A reasonable agreement is seen between LES and the measurement and between the caster and water model.

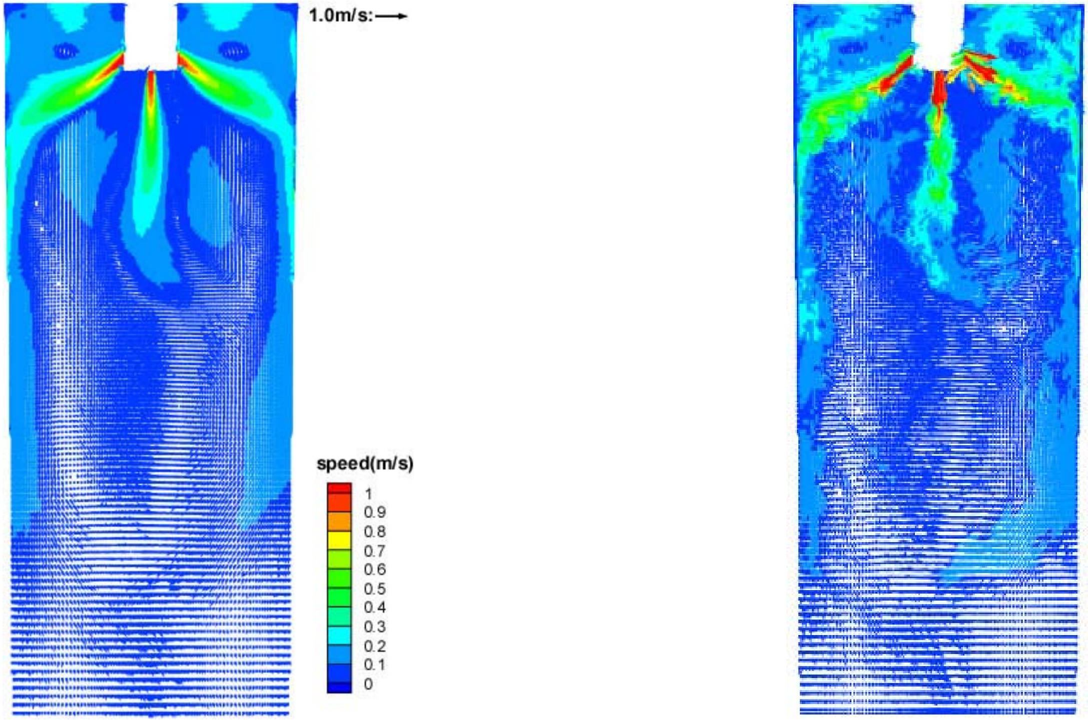

(a) (b)

Fig. 6: LES predicted velocity vectors at the center plane of the steel caster.

Comparison of the Water Model and Steel Casting Machine

Differences between the water model and real steel casting machine are shown in Figures 8 and 9, which compare the time averaged downward flow velocity and its *rms* for the water model and casting machine along a horizontal line 1000mm below the top surface and 164mm from the narrow face. The data are averaged over 48.5 and 51 seconds for the water model and casting machine respectively. Figure 8 shows a bigger spatial variation of the downward velocity for the water model. It also shows that the steel casting machine has less upward (or reverse) flow. Two main reasons are suspected to cause this: the tapering and solidification restricts the flow domain, which hastens the even distribution of the flow; and the downward withdrawal of the shells discourages the flow from having upward velocities. An asymmetry between the two sides can also be seen for the water model and casting machine, implying that a low frequency oscillation between the two sides exists and 51 seconds are not enough for the time average.

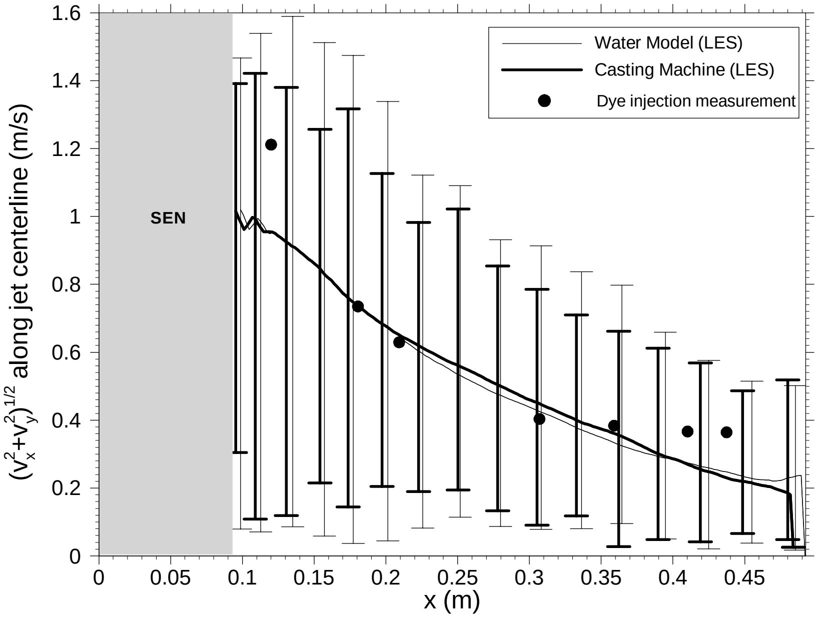

Fig. 7: Speed along jet centerline, comparing LES and dye injection measurements (full-scale water model).

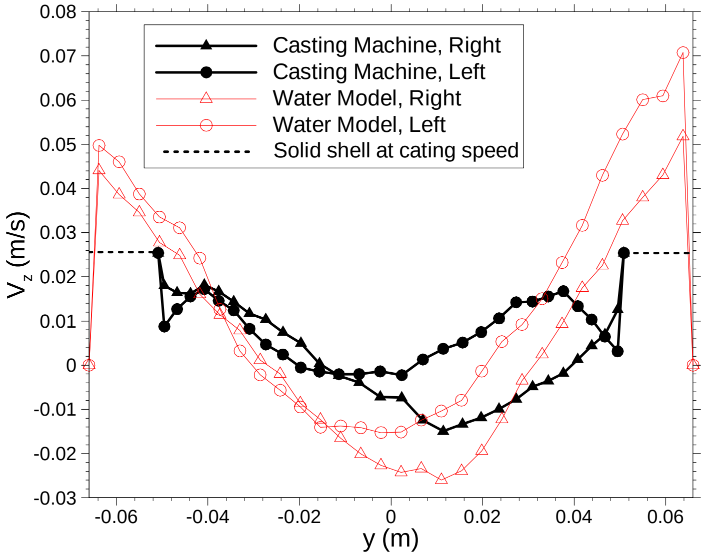

Fig. 8: Comparison of downward velocities through thickness of the full-scale water and casting machine near narrowfaces.

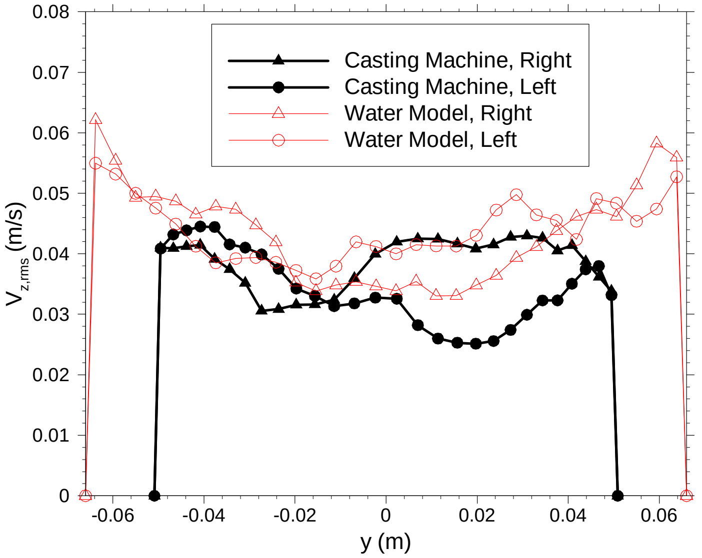

Fig. 9: Comparison of fluctuations of the downward velocities in Fig. 8.

Top Surface Fluctuations

Figure 10 (a) shows the time-variation of the horizontal velocity towards the SEN at the center points between the SEN and the narrowface on the top surface, obtained from the steel caster simulation. As also shown deeper in the caster (Fig. 9), the velocity fluctuations are very large – similar to the velocity magnitude. Figure 10(a) shows a large component with high frequency (e.g. flow velocity drops from ~0.4m/s towards the SEN to a velocity in the opposite direction within 0.2s). Due to lack of long-term measurement of this velocity time-variation for this steel casting machine or water model, this result is compared with our previous PIV measurement on a 0.4-scale water model, which was published elsewhere [18] and is presented in Fig. 10(b). Figure 10(b) also shows LES data obtained from half-mold simulations of the 0.4-scale water model, assuming symmetrical flow in each half. The same large component in high-frequency as observed in the steel caster simulation is also seen in the measurements but missing in the half-mold simulations. This suggests that interaction between the two sides of the caster is the cause of the large high frequency fluctuations. The variations are significant, because the level fluctuations which accompany them are a major cause of defects in the process.

Top Surface Level

Top surface level is important because it affects the liquid flux ability to fill the interfacial gap between the mold and shell, which is important to heat transfer and surface quality. Figure 11 shows typical transient top surface levels obtained from the simulation. Figure 11(a) shows the water model prediction compared with measured top surface levels on video at three instants. It is seen that the prediction agrees with the measurements reasonably. Figure 11(b) presents the predicted steel caster top surface level. The level is always higher near the narrowfaces, by 2mm and 4-6mm for the water model and steel caster respectively. This is because the steel upward momentum near the narrowfaces lifts the liquid level there, displacing some of the molten flux. The flux layer must be thick enough to cover the steel, in order to provide a steady supply of molten flux into the interfacial gap to lubricate the steel. Insufficient flux consumption leads to temperature fluctuations which cause surface cracks and other defects in the solid steel product. Thus, the height of the surface “standing wave” is important to steel quality. The prediction of the steel caster top level here compares reasonable with industry measurements using nail boards and sheets (Fig. 11(b)). Uncertainty in the measurement exists regarding possible rotation of the sheet.

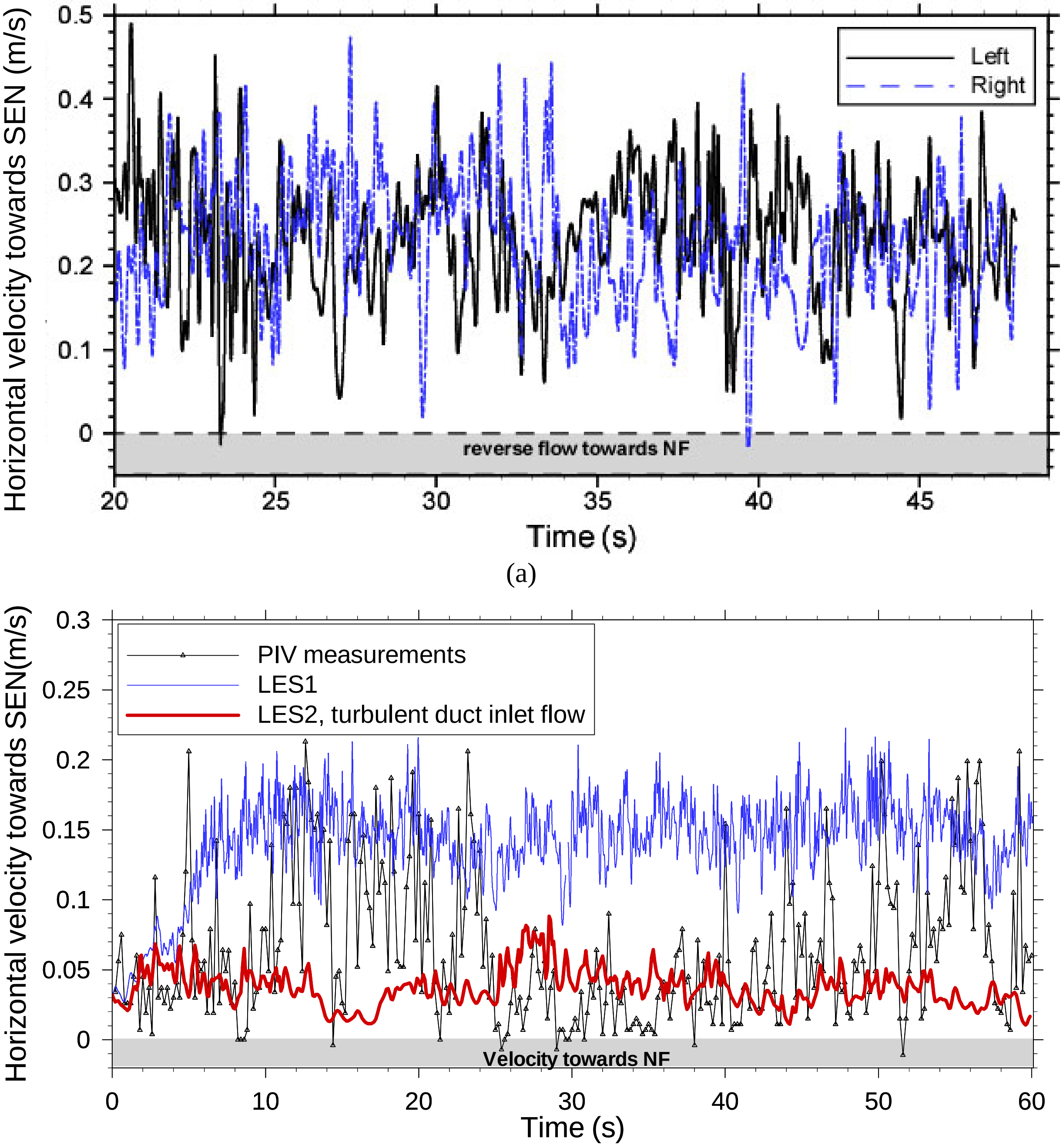

(a)

(b)

Fig. 10: Time variation of horizontal velocity towards SEN at the center points of the top surface of the (a) steel caster and (b) 0.4-scale water model.

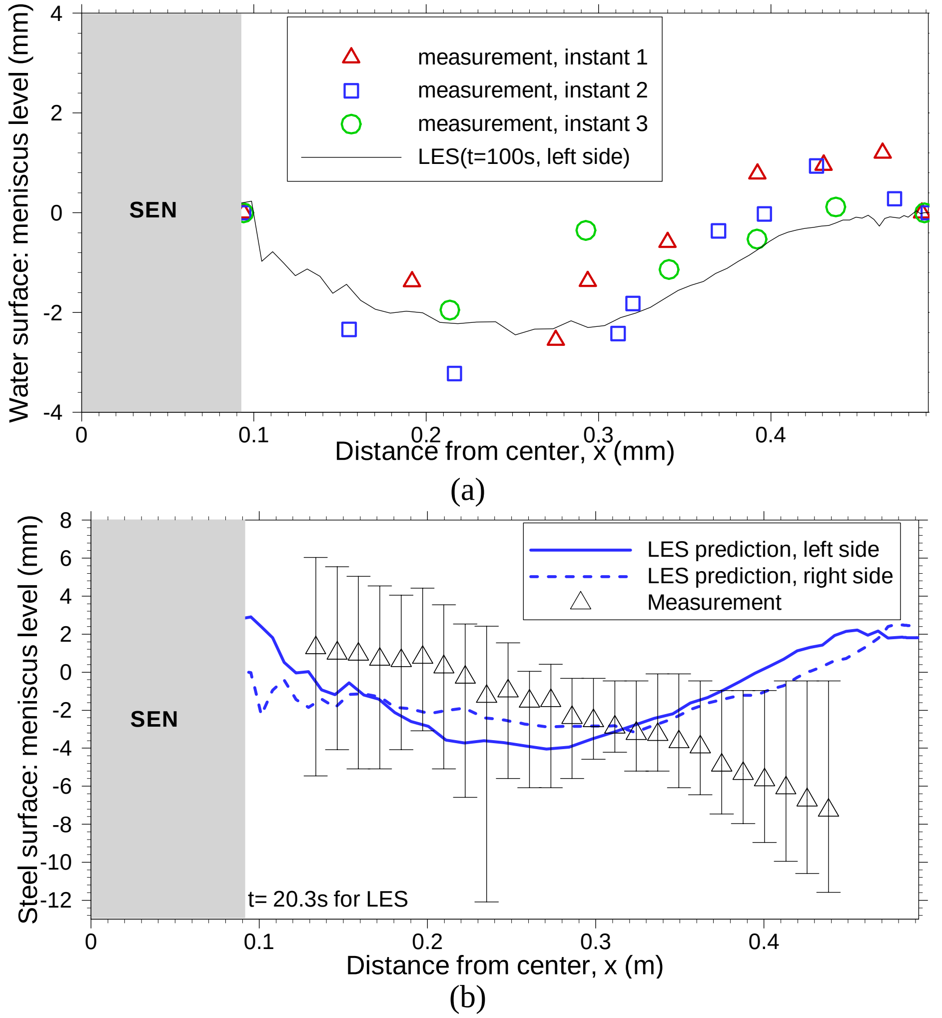

Fig. 11: Typical instantaneous top level approximated from the computed pressure by $(\frac{(p-p_{mean})}{(\rho_{steel}-\rho_{flux})g})$, obtained from LES compared with measurements for (a) the full-scale water model, (b) the steel caster.

PARTICLE TRANSPORT RESULTS

Particle Entrapment Modeling

Engulfment and entrapment are two basic mechanisms by which inclusions are captured by the dendritic solidification front [19-23]. Engulfment occurs when the dendrite growth speed exceeds a critical velocity. Under this condition, particles cannot escape fast enough from being surrounded by the approaching front and are captured inside the dendrites. Entrapment occurs when the particles are surrounded by the growing dendrite arms and get captured in between them. Fundamental criteria have been developed for the capture of inclusions by a moving dendritic interface through engulfment or entrapment in this project, considering together for the first time: critical dendrite growth velocity, particle size, primary dendrite arm spacing (PDAS) and local cross-flow velocity. The model includes the effects of surface tension, multidirectional drag, Saffman lift, buoyancy and friction forces. Particles smaller than the PDAS are predicted to become surrounded by the dendrite arms and entrapped with little chance of "particle pushing" [19-23]. Figure 12 presents the measured PDAS for the simulated steel slabs [16], showing increasing PDAS for both wide and narrow faces with depth below the top surface. The smallest PDAS is found near the top surface to be around 50µm, hence the particle sizes of this work (10µm and 40µm) can be safely modeled as entrapped by the shell when they ever touch a domain wall.

Particle Transport

Figure 13 shows the particle distribution and entrapment locations at three instants for the mold and flow conditions discussed in the flow results section. Particles are seen to move with the jet and reach the narrowface 0.6 seconds after injection at 33 seconds. The particles split into two groups by 2 seconds (the middle frame) and enter the upper and lower rolls. Although the flow and particle distribution exiting the nozzle ports is initially almost symmetrical, a significant asymmetry can be seen to develop in the 48 seconds plot (15 seconds after injection), indicating the important effects of flow asymmetry on particle transport. It is important to note that the inlet velocity distribution was relatively uniform during this time, so the asymmetry in this case is caused solely by chaotic turbulent motion below the jet. This can be seen from Fig. 14, which shows time-variations of the downward velocity at two pairs of symmetrical monitoring points on each side of the domain. The first pair (red triangles) is located on the jet to monitor the flow differences between the jets on two sides. The second pair (purple diamonds) is 1.2m below the top surface and near narrowfaces to investigate the flow in the lower roll zones. Data in Fig. 14 clearly support the above discussion. The downward motion corresponds to large asymmetry between the velocities at the second pair of points, showing that the particle transport is dominated by the flow distribution, regardless of particle size. The velocities in Fig. 14 are also seen to fluctuate, indicating that particles injected at other times will show the opposite asymmetry or behave almost the same. These results are important because particles, which are transported deeper, are more likely to become permanently entrapped in the steel caster.

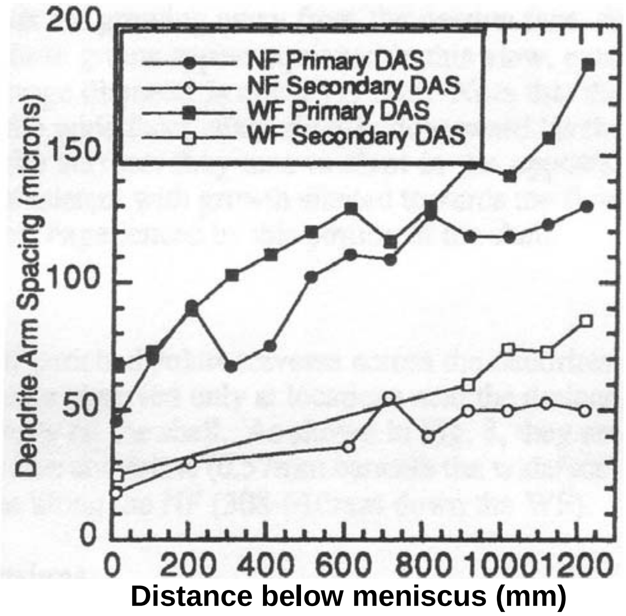

Fig. 12: Variation of primary dendrite arm spacing (PDAS) along distance below meniscus [16].

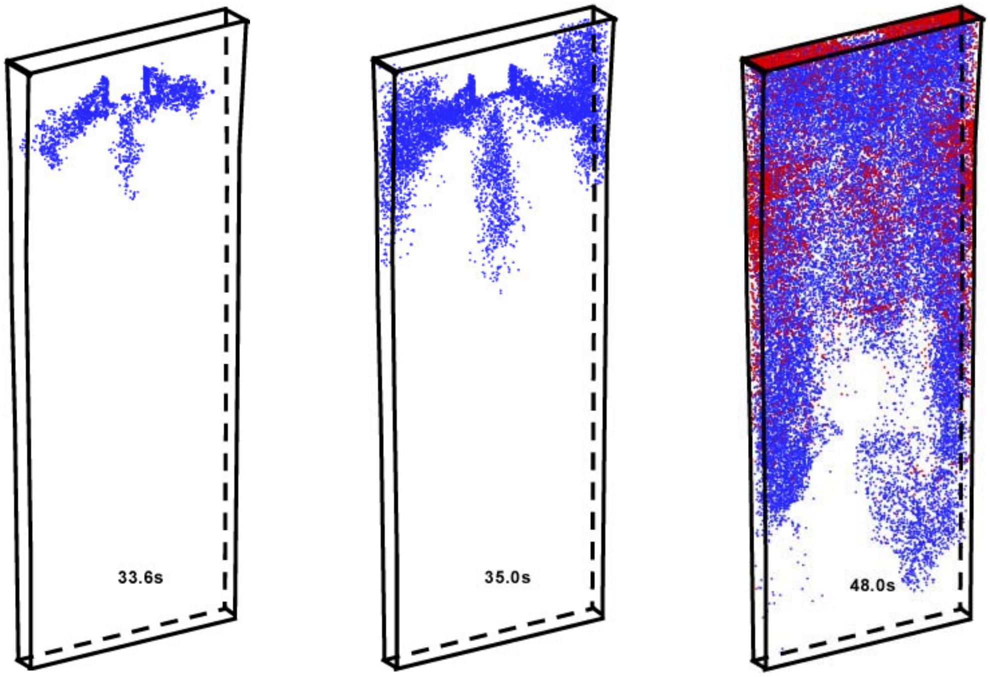

Fig. 13: Particle distributions at three instants (blue dots are moving particles; red dots are entrapped particles by solidifying shell).

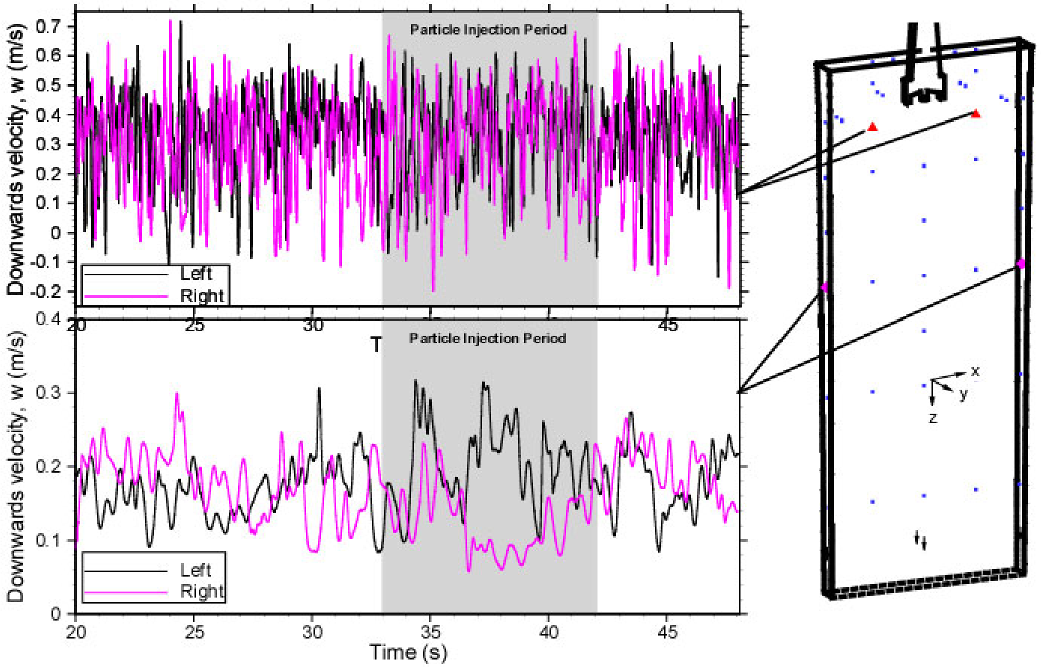

Fig. 14: Time variations of downward velocity at two points showing inherent transient asymmetry of the lower rolls.

Figure 15 shows the measured asymmetry distribution of particle entrapment of some other steel casting machine by Jacobi [24]. He suspects that the asymmetrical flow exiting the nozzle ports, caused by the asymmetrical clogging in the SEN, is the main cause of the asymmetrical defects in the final steel strands (as shown in the figure). The present work, however, shows that flow asymmetries in the lower roll zone are an inherent feature of chaotic mold flow, which can lead to asymmetrical particle transport and entrapment, even for almost symmetrical jet flows. Techniques such as electromagnetic braking or better nozzle design required to prevent particles from getting into the lower roll zone are suggested to reduce the particle related defects.

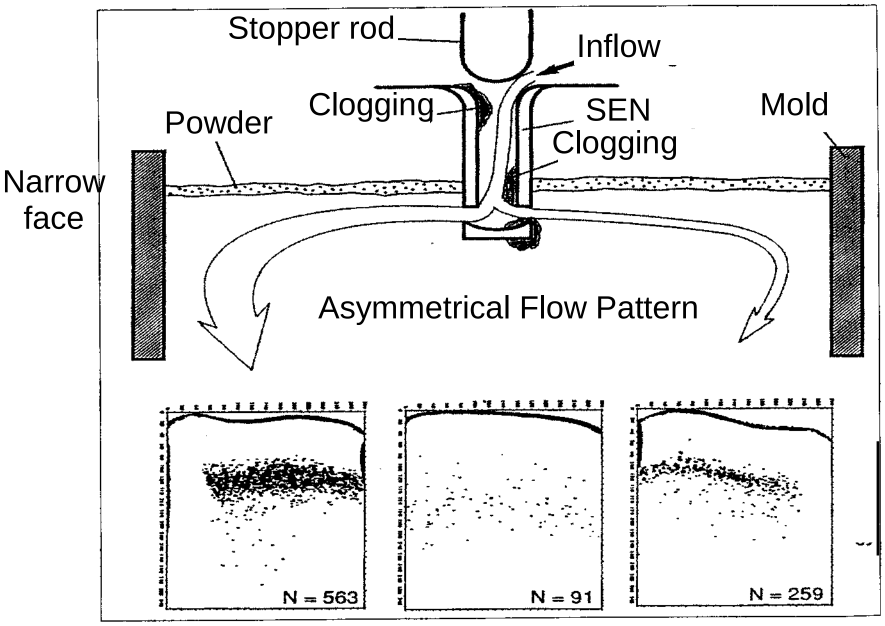

Fig. 15: Asymmetrical inclusion defects found in steel products [24].

Figure 16 shows five computed typical particle trajectories for 60 seconds or until they contact the top surface. The green trajectory (labeled 1) shows a particle that exists the left nozzle port, recirculates along the upper roll and eventually gets removed at the top surface. The red trajectory (2) shows a particle entering the mold from the center port, floating into the left side as the center jet spreads and finally getting moved to the top surface on the right side. The purple and blue trajectories (3 and 4) show particles flowing out of the domain after floating between the upper and lower rolls or moving with the flow directly into the lower region. These particles will most likely be entrapped in the final product. The black trajectory (5) shows a particle that gets entrapped on the wideface ~0.8m below the top surface. These irregular trajectories show some random motions and provide evidence for the effect of the turbulent fluid structures on particle transport.

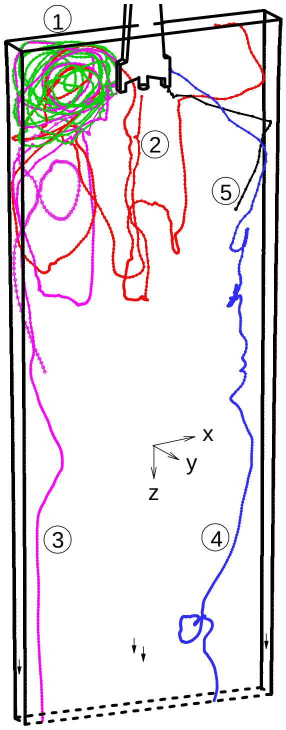

Fig. 16: Predicted typical particle trajectories in steel caster mold region (LES).

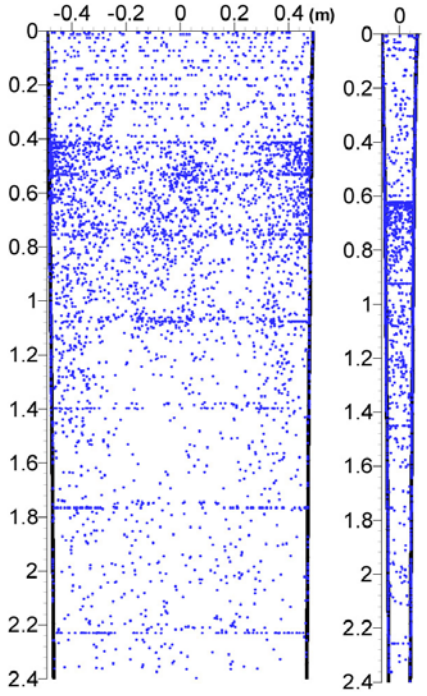

Fig. 17: Distribution of particle entrapment locations in wideface (left) and narrowface (right).

Figure 17 shows the 4263 entrapment locations of the 10,000 10μm 5000Kg/m^3 particles for the 60 seconds. Most of the particles are trapped 0.5-0.8m below the top surface. The slight banding effect is due to the stair-case mesh of the shell so should be ignored. In contrast with bifurcated nozzles, there is a slight concentration of particles trapped beneath the central port, in addition to concentrations near the narrowfaces. No major differences are seen among the four particle groups. This suggests that particles smaller than a certain critical size (predicted here to be larger than 40μm) behave in the same way in the mold region. A slight asymmetry of particle entrapment location can also been seen in the wideface view, which is consistent with the asymmetrical particle transport shown in Fig. 13.

CONCLUSIONS

Advanced computational models (LES) are being developed to predict quantitatively the chaotic turbulent flow and the transport and removal of inclusions in the mold region during the continuous casting of steel. The following findings have been obtained from the present work:

1) The computed velocity field agrees quantitatively with the measurement. The top surface level can be reasonably predicted from the computed pressure distribution across the top surface;
2) Water models are generally representative of steel casters. However, steel casting machines are likely to have more evenly distributed downward flow in the lower roll zone.

3) The interaction between the left and right sides of the caster produces asymmetric flow, which is significant both at the top surface (influencing velocity fluctuations and standing wave), and in the lower roll zone (influencing inclusion entrapment to the shell);
4) Particle transport is governed by the fluid flow pattern, leading to asymmetric entrapment profiles, which can be predicted with the transient model presented here.

APPENDIX: Mathematical Modeling

Fluid Flow

The time-dependent three-dimensional Navier-Stokes equations have been solved for the fluid velocity field.

$$\frac{\partial \mathrm{v}_i}{\partial x_i} = 0 \tag{1}$$

$$\frac{D\mathrm{v}_i}{Dt} = -\frac{1}{\rho}\frac{\partial p}{\partial x_i} + \frac{\partial}{\partial x_j}\nu_{eff}\left(\frac{\partial \mathrm{v}_i}{\partial x_j} + \frac{\partial \mathrm{v}_j}{\partial x_i}\right) \tag{2}$$

In both simulations of this work, because of the relatively fine computational mesh (please see the computational details section), no sub-grid scale (SGS) models were employed, so the two simulations are also called coarse grid DNS (direct numerical simulation).

Particle Transport

The Lagrangian approach is employed for particle transport. The governing equations of particle motion are:

$$\mathrm{v}_{p,i} = \frac{dx_{p,i}}{dt} \tag{3}$$

$$\frac{d\mathrm{v}_{p,i}}{dt} = \frac{18\rho\nu_0}{\rho_p d_p^{\ 2}}\left(1 + 0.15\,\mathrm{Re}_p^{\ 0.687}\right)\left(\mathrm{v}_i - \mathrm{v}_{p,i}\right) + (1 - \frac{\rho}{\rho_p})g_i + 6.64\mu_0\left(\frac{d_p}{2}\right)^2 \left|\mathrm{v} - \mathrm{v}_p\right|\sqrt{S_{avg}/\nu_0} \tag{4}$$

where in Eqn.(4), the first term on the right hand side is the drag force acting on the particle because of the velocity difference between the particle and its surrounding fluid, the second term is the gravity and buoyancy forces, and third term is the Saffman lift force. Re_p is the relative Reynolds number of the creeping flow around the particle defined by

$$\mathrm{Re}_p = \frac{\left|\vec{\mathrm{v}}_p - \vec{\mathrm{v}}\right| d_p}{\nu_0} \tag{5}$$

Computational Details

In this present work, the transient 3D Navier-Stokes equations are discretized using the Harlow-Welch fractional step procedure. Second order central differencing is used for the convection terms and the Crank-Nicolson scheme is used for the diffusion terms. The Adams-Bashforth scheme is used to discretize in time with second order accuracy. The pressure Poisson equation is solved using an Algebraic multi-grid solver. Computational grids consisting of 0.7 million and 1.3 million cells are used for the two computations of this work respectively. The time steps for the fluid flow simulations are 0.001 seconds. The LES computation takes 29.5 CPU seconds per time step on a Pentium IV 1.7GHz PC with the 1.3 million cells mesh or 24 days for 70,000 time steps (70 seconds of real time).

The particle transport equations are integrated for each particle using a fourth order Runge-Kutta method at the same time as the velocity field is computed. Four groups of 10,000 alumina particles are studied in this present work, with the particle properties showing in Table II. The integrating time steps for particle simulation are smaller than 0.001 second and vary for different property particles (to keep the simulation stable), due to their different momentum response times. The smallest particle integrating time step is 2×10^{-6} seconds (i.e. 500 time steps for particle motions are performed inside each fluid flow simulation time step). The simulation of the 40,000 particles slows down the computational speed by a factor of two.

Table II. Properties and conditions of particle transport computation.

Particle Group Index	Particle Diameter (μm)	Particle Density (Kg/m^3)	Response Time (μs)
1	40	2700	42.8
2	40	5000	79.3
3	10	2700	2.68
4	10	5000	4.96

NOMENCLATURE

$\frac{D}{Dt}$	total derivative $(=\frac{\partial}{\partial t}+\mathrm{v}_j\frac{\partial}{\partial x_j})$
$\vec{x}$	displacement vector
$\vec{\mathrm{v}}$	velocity vector
μ_0	laminar dynamic viscosity of fluid
ν_0	laminar kinematic viscosity of fluid
ν_{eff}	effective viscosity of fluid
ρ	fluid density
ρ_p	particle material density

d_p	particle diameter
p	statistic pressure
S_{avg}	local velocity gradient of the shear flow
t	time
$\vec{g}$	gravity vector

Subscripts:

i	directions (x, y, z)
p	particle

ACKNOWLEDGEMENTS

The authors thank the National Science Foundation (Grant DMI-01-15486) which made this research possible. The work is also supported by the member companies of the Continuous Casting Consortium at University of Illinois at Urbana-Champaign (UIUC). Special thanks are due to Ya Meng for calculating the shell thickness and National Center for Supercomputing Applications (NCSA) at UIUC for computational facilities.

REFERENCES

1. J. Herbertson, Q.L. He, P.J. Flint, R.B. Mahapatra, "Modelling of Metal Delivery to Continuous Casting Moulds," in Steelmaking Conf. Proceedings, Vol. 74, ISS, Warrendale, PA, 1991, 171-185.
2. B.G. Thomas and L.M. Mika, "Simulation of Heat Transfer and Fluid Flow Inside a Continuous Slab Casting Machine," Second FIDAP Users Conference, (Evanstan, IL), Fluid Dynamics International Inc., 500 Davis Ave., Suite 400, Evanston, IL, 1988, 1-29.
3. B.G. Thomas, L.M. Mika and F.M. Najjar, "Simulation of Fluid Flow Inside a Continuous Slab Casting Machine," Metall. Trans. B, Vol. 21B, 1990, 387-400.
4. B.G. Thomas and F.M. Najjar, "Finite-Element Modeling of Turbulent Fluid Flow and Heat Transfer in Continuous Casting," Applied Mathematical Modeling, Vol. 15, 1991, 226-243.
5. B.G. Thomas, F.M. Najjar and L.J. Mika, "The Removal of Superheat from Continuous Casting Molds," Proc. F.Weinberg Int. Symposium on Solidification Processing, 29th Canadian Inst. Min. Met. Conf., (Hamilton, Ontario), Pergamon Press, Inc., Toronto, 1990, 131-145.
6. B.G. Thomas, Q. Yuan, S. Sivaramakrishnan, T. Shi, S.P. Vanka, M.B. Assar, "Comparison of four Methods to Evualuate Fluid Velocities in a Continuous Casting Mold," ISIJ International, Vol. 41 (10), 2001, 1262-1271.
7. B.G. Thomas and L. Zhang, "Mathematical Modeling of Fluid Flow in Continuous Casting," ISIJ International, Vol. 41 (10), 2001, 1181-1193.

8. S. Sivaramakrishnan, H. Bai, B.G. Thomas, P. Vanka, P. Dauby, M. Assar, "Transient Flow Structures in Continuous Cast Steel," in Ironmaking Conference Proceedings, Vol. 59, ISS, Warrendale, PA, (Pittsburgh, PA), 2000, 541-557.
9. Q. Yuan, S.P. Vanka and B.G. Thomas, "Large Eddy Simulations of Turbulent Flow and Inclusion Transport in Continuous Casting of Steel," 2nd International Symposium on Turbulent and Shear Flow Phenomena, June 27 - 29, 2001, Royal Insitute of Technology(KTH), Stockholm, Sweden, 2001, 6.
10. K. Takatani, Y. Tanizawa, H. Mizukami, K. Nishimura, "Mathematical Model for Transient Fluid Flow in a Continuous Casting Mold," ISIJ International, Vol. 41 (10), 2001, 1252-1261.
11. R.C. Sussman, M. Burns, X. Huang, B.G. Thomas, "Inclusion Particle Behavior in a Continuous Slab Casting Mold," in 10th Process Technology Conference Proc., Vol. 10, Iron and Steel Society, Warrendale, PA, (Toronto, Canada, April 5-8, 1992), 1992, 291-304.
12. S. Sivaramakrishnan, B.G. Thomas and S.P. Vanka, "Large Eddy Simulation of Turbulent Flow in Continuous Casting of Steel," in Materials Processing in the Computer Age, Vol. 3, V. Voller and H. Henein, eds., TMS, Warrendale, PA, 2000, 189-198.
13. M.B. Assar, P.H. Dauby and G.D. Lawson, "Opening the Black Box: PIV and MFC Measurements in a Continuous Caster Mold," in Steelmaking Conference Proceedings, Vol. 83, ISS, Warrendale, PA, 2000, 397-411.
14. B.G. Thomas, R. O'Malley, T. Shi, Y. Meng, D. Creech, D. Stone, "Validation of Fluid Flow and Solidification Simulation of a Continuous Thin Slab Caster," in Modeling of Casting, Welding, and Advanced Solidification Processes, Vol. IX, Shaker Verlag GmbH, Aachen, Germany, (Aachen, Germany, August 20-25, 2000), 2000, 769-776.
15. R.J. O'Malley, "Observations of Various Steady State and Dynamic Thermal Behaviors in a Continuous Casting Mold," 82nd Steelmaking Conference, (Chicago, IL), TMS, 1999, 21.
16. B.G. Thomas, R.J. O'Malley and D.T. Stone, "Measurement of temperature, solidification, and microstructure in a continuous cast thin slab," Modeling of Casting, Welding, and Advanced Solidification Processes, (San Diego, CA), TMS, Warrendale, PA, Vol. VIII, 1998, 1185-1199.
17. Y. Meng and B.G. Thomas, "Heat Transfer and Solidification Model of Continuous Slab Casting: CON1D," Metallurgical and Materials Transactions B, Vol. (submitted on Aug. 23), 2002,
18. Q. Yuan, T. Shi, B.G. Thomas, S.P. Vanka, "Simulation of Fluid Flow in the Continuous Casting of Steel," Proceedings: Computational Modeling of Materials, Minerals and Metals Processing, (Seattle, WA), TMS (The Materials, Minerals and Metals Society), 2001, 491-500.
19. D. Shangguan, S. Ahuja and D.M. Stefanescu, "An Analytical Model for the Interaction between an Insoluble Particle and an Advancing Solid/Liquid Interface," Metallurgical Transactions A, Vol. 23A (2), 1992, 669-680.
20. J. Potschke and V. Rogge, "On The Behavior of Foreign Particle at An Advancing Solid-Liquid Interface," Journal of Crystal Growth, Vol. 94, 1989, 726-738.
21. D.M. Stefanescu and A.V. Catalina, "Calculation of The Critical Velocity for The Pushing/Engulfment Transition of Nonmetallic Inclusions in Steel," ISIJ International, Vol. 38 (5), 1998, 503-505.
22. G. Wilde and J.H. Perepezko, "Experimental Study of Particle Incorporation during Dendritic Solidification," Materials Science & Engineering A, Vol. 283, 2000, 25-37.
23. Y. Wang, M. Valdez and S. Sridhar, "Liquid and Solid Inclusions at Advancing Steel Solidification Fronts," Z. Metallkd., Vol. 93 (1), 2002, 12-20.
24. H. Jacobi, H.-J. Ehrenberg and K. Wuennenberg, "Development of the cleanness of different steels for flat and round products," Stahl und Eisen, Vol. 118 (11), 1998, 87-95.